Biophysical Society

Force measurements of Myosin II waves at the yolk surface during *Drosophila* dorsal closure

Lara Selvaggi,[1,2] Mirco Ackermann,[1] Laurynas Pasakarnis,[2] Damian Brunner,[2] and Christof M. Aegerter[1,2,*]
[1]Physik-Institut, Universität Zürich, Zürich, Switzerland and [2]Department of Molecular Life Science, Universität Zürich, Zürich, Switzerland

ABSTRACT   The mechanical properties and the forces involved during tissue morphogenesis have been the focus of much research in the last years. Absolute values of forces during tissue closure events have not yet been measured. This is also true for a common force-producing mechanism involving Myosin II waves that results in pulsed cell surface contractions. Our patented magnetic tweezer, CAARMA, integrated into a spinning disk confocal microscope, provides a powerful explorative tool for quantitatively measuring forces during tissue morphogenesis. Here, we used this tool to quantify the in vivo force production of Myosin II waves that we observed at the dorsal surface of the yolk cell in stage 13 *Drosophila melanogaster* embryos. In addition to providing for the first time to our knowledge quantitative values on an active Myosin-driven force, we elucidated the dynamics of the Myosin II waves by measuring their periodicity in both absence and presence of external perturbations, and we characterized the mechanical properties of the dorsal yolk cell surface.

SIGNIFICANCE   The intent of this research was the study of force-regulated processes in biological organisms, with emphasis being placed on the fundamental relations between the generation of forces and the associated mechanical response during tissue morphogenesis in embryos of *Drosophila melanogaster*. We developed an automated and microscope-compatible device that uses a magnetic field to apply forces to micrometer-sized magnetic beads while using video bead tracking to measure cell-generated molecular forces and mechanical properties in living organisms. The design and the approach we have established here can be also applied widely in other organisms for analyzing cell or embryo functions affected by cytoskeletal forces.

INTRODUCTION

Drosophila melanogaster is a versatile model organism used to study a broad range of biological processes including cell and tissue morphogenesis (1). The ready availability of genetic perturbations in *Drosophila*, and the amenability to live imaging of morphogenetic processes, allows their space- and time-resolved monitoring and their comparative analysis in wild-type and mutant embryos.

Tissue closure and fusion is a common morphogenetic process in the development of all organisms and its disruption leads to a variety of defects (2). In addition, tissue closure and fusion are also central to wound healing (3). Dorsal closure (DC) is one of the best studied tissue closure and fusion events taking place during stages 13 and 14 of *Drosophila* em-bryonic development (4). During DC a large opening of the epidermis tissue closes and seals through the action of multiple forces. The amnioserosa tissue that fills the opening and is attached to the surrounding epidermis, produces the key pulling force converging the flanking epidermis fronts dorsally (5). Thereby, each amnioserosa cell gradually constricts its apical surface while changing from a flat to a bottle-like shape. As a consequence the tissue surface curves inward and eventually rolls up into a tube, allowing the epidermis fronts to zip up over it and seal the opening (6).

The contractile forces driving apical constriction of amnioserosa cells were shown to be pulsed (7). Thereby, transient, locally appearing F-actin densities form and often move wave-like across the cell surface (8). The densities eventually contract via the action of Myosin II motors and then disappear. In the meantime, such pulsed contractility was found to drive multiple morphogenetic processes also in vertebrates and mammals, among others neurulation, which is a process closely related to DC (9,10), showing the interest in being able to determine the properties of

such contractile forces in general. Being able to arrest the Myosin II dynamics in the amnioserosa tissue (5), we are able to observe similar contractile Myosin II waves on the surface of the yolk cell, which we will study here as a proxy of such contractile cellular forces.

In the past, considerable effort was undertaken to derive a measure for the forces produced by cells, in particular during cell migration and during morphogenetic processes. However such measurements are not straightforward, and generally, numbers had to be deduced indirectly. Several force measurement techniques using, e.g., optical tweezers (11), magnetic forces (12), or atomic force microscopy (13), as well as nonmechanical observation techniques (14), working at cellular and tissue levels, have been used and combined, also to locally infer the force involved during tissue morphogenesis (7), but a quantitative value of the force responsible for such a process is a point that remains to be addressed.

More recently, force spectroscopy methods opened the possibility to study biological processes regulated by mechanical forces. The power and versatility of these techniques are highlighted by the number of applications and systems to which they have been applied (15). The decision as to which of these techniques is suited for a particular measurement is mainly determined by the relevant range of forces and displacements, as well as the required spatial and temporal resolution. Magnetic tweezers (MT) have several advantages over other force spectroscopy techniques such as the absence of photo-toxicity, a higher selectivity in trapping the probe particle, and the possibility to apply relatively large forces. All of these make the use of MT much more attractive compared with optical tweezers or atomic force microscopy (16). In addition, such methods have a potential to be applied in the study of morphogenetic processes in living organisms, where force measurements are particularly challenging. Consequently, absolute values of the cellular forces driving morphogenetic processes, such as tissue closure, are not known, although they would be crucial for a comprehensive understanding. Here we employed our patented MT, CAARMA, to measure forces (17). Due to its compact size, CAARMA was conveniently mounted on the stage of an inverted spinning disk microscope and used to apply magnetic forces on 4.5-μm Dynabeads, injected into the yolk cell of stage 5 embryos. We then measured the force exerted on the beads by Myosin II waves that we had found to migrate across the dorsal yolk cell surface of stage 13 and 14 embryos. The analyzed Myosin II waves became readily visible in mutant stage 13 embryos, in which we had arrested dorsal closure by amnioserosa tissue-specific interference with Myosin II activity (5). We found these waves to produce forces in the nN range and to dynamically change in response to externally applied perturbation forces up to 1.6 nN. In a specified location the waves appear with a certain periodicity that decreased over time. Finally, we studied the mechanical response of the yolk cell by performing pulling and release experiments on its cortex. Because the resistance to deformation can arise not only from the mechanical properties of the

cortical elements, but also from the viscoelastic cytoplasm, we also measured the microrheological properties of the cytoplasm in stage 13 yolk cells, as previously done in *Drosophila* embryos during the first, syncytial blastoderm stage of development (17). The resulting viscosity value was about 25 times larger than that of the syncytial blastoderm cytoplasm. Similarly, the elastic modulus of the stage 13 yolk cell cortex was three orders of magnitude higher than that before cellularization.

MATERIALS AND METHODS

Fly strain and embryos preparation

To observe the Myosin II waves on the surface of the yolk cell, we had to prevent the progression of dorsal closure by interfering with AS cell contraction. To obtain that we crossed the fly strains sqh:sqh:GFP:UAS-slmb and 332.3 Gal4 (5), with mCherry-tagged Sqh for imaging the Myosin II activity in the yolk cell. The binary Gal4-UAS system is a method for driving gene expression in a spatiotemporal controlled manner (18). It is a routinely used method for directing the expression of a gene of interest to a specific tissue in *Drosophila melanogaster* (19). Collection, dechorionation, and preparation of *Drosophila* embryos for microinjection was done according to the standard protocol (20).

Single bead injection into the yolk cell

A single magnetic bead is injected into the yolk cell of an embryo at the cellular blastoderm stage 5, immediately after cellularization. Beads are 4.5 μm in diameter with a mass saturation magnetization of 19.6 Am^2/kg (Dynabeads M-450, Thermofisher, Waltham, MA). To avoid bead aggregation and reduce electrostatic interaction with the glass walls of the injection needle, 1 mL of beads (4 x 10^8 beads/ml supplied in distilled water) was incubated for 15 min with 1:1000 Tween-20/water solution. The beads were then washed three times with de-ionized water and suspended in 200 μL of de-ionized water before injection. Injections were carried out using an upright Zeiss Axiovert X35 microscope equipped with a Narishige MO-11 injection manipulator (Narishige Scientific Instrument Lab, Setagaya-ku, Tokyo, Japan). To generate the injection needles, borosilicate capillaries (GC100TF-10, Harvard Instruments, Holliston, Massachusetts) were pulled using a Narishige needle puller PN-3 (Narishige Scientific Instrument Lab). The needle mounted on the injection manipulator was broken by pushing against the side of the glass slide to produce an opening corresponding to ~2 bead diameters (~10 μm). Instead of traditionally loading the injection needle with beads solution, we place the needle into a drop of beads solution and sucked up few individual beads, with some space in between. The beads are therefore arranged in a line close to the tip, and a light pressure is sufficient to eject them, one at a time. In this way we reduced the following: 1) the unwanted amount of water we inevitably inject with the beads and 2) clogging issues due to multiple beads simultaneously exiting the opening upon applying pressure. Following this procedure, we were able to efficiently inject a single bead into the yolk cell. After injection, the coverslip holding the embryos with their dorsal side facing down was placed on a neodymium permanent magnet to pull the beads dorsally.

Experimental setup

The experimental setup consists of the patented MT, CAARMA, designed in our lab (http://www.caarma.info). The MT is mounted on an aluminum frame that can be easily integrated into commercial microscopes. We mounted it onto a Leica spinning disk confocal microscope
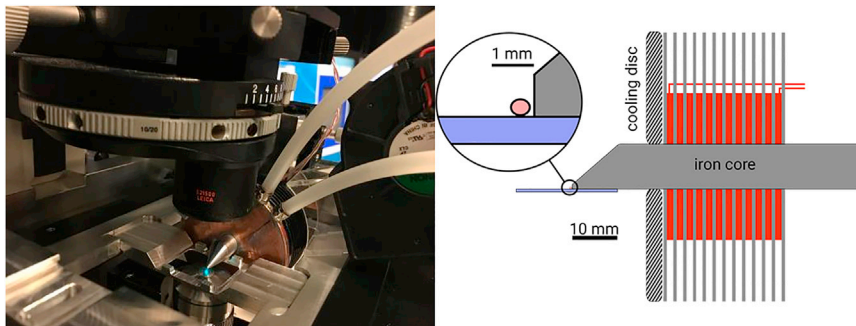
FIGURE 1 CAARMA integrated on a Leica spinning disk confocal microscope to perform force measurements.

(Fig. 1), to have the capability of exerting controlled forces in vivo, while studying the structural changes and the mechanical response during tissue morphogenesis in developing *Drosophila* embryos. The electromagnet design and its cooling system have been previously described in detail (17).

Briefly, a magnetic field gradient is generated by a copper coil wrapped around an iron core, exhibiting an asymmetric tip similar, in shape, to the head of an airplane with a flat base and a convergent top profile, as described in Selvaggi et al. (17). The flat base of the tip allows the magnet to sit on the coverslip and come close the embryo, while a convergent profile of the top part guarantees a high magnetic flux gradient in the area of interest. Other advantages using the asymmetric core profile include the following: the possibility to employ a short working distance objective lens, as the latter can be moved unimpeded underneath the coverslip; the capability of applying horizontal forces perpendicular to the sample, which is very convenient for tracking analysis as no other components must be considered; and the capability of exerting constant forces by using only a single electromagnet, which allows working at long bead-core distances, where the nonlinearity of the force-distance relationship is not very pronounced. For imaging the samples, we used a 63X oil-immersion objective, and to record data we used an iXon3/888 sCMOS Andor Camera with an acquisition frame rate of 6.62 fps. In addition, we developed a tracking software for data analysis. It detects, tracks, and records bead displacement, and from this calculates position and speed of the particles, thus determining the force acting on it. The device we developed is very versatile and suitable for a range of other applications.

Force calibration

To determine the magnitude of the applied forces, we first calibrated our MT using the drag method. This force calibration procedure allows determining the force as a function of the distance from the magnetic tip and as a function of the electric current provided to the coil. Theoretically, the applied force could also be determined based on these parameters as well as the magnetic properties of the bead used as a probe (21). In particular, the magnetic force scales with the magnetic moment of the bead in addition to the magnetic field strength at the position of the bead. Consequently, the volume of magnetic material present in the bead and the magnetic susceptibility are relevant factors affecting force magnitudes.

To calibrate our MT, we used a borosilicate glass capillary with a square cross section (Friederich & Dimmock, Millville, NJ), an outer width of 500 μm, and a wall thickness of 100 μm. We filled the capillary with 4.5-μm Dynabeads diluted in a 90% glycerol-water solution. The density of the magnetic beads was kept very low: magnetic beads were spaced by about 10 diameters from each other. In Fig. 2, we show the force calibration curves for different current values, as indicated in the legend. These curves were obtained by using the drag method.

The position of a magnetic bead was tracked, relative to the magnetic tip, through a stationary fluid of known viscosity. For micro-beads, the viscous

drag dominates over all other hydrodynamic effects and the flow is laminar. In addition, due to the low density of beads, no additional hydrodynamic shielding forces reducing the drag are present. In this regime, a spherical bead will move in response to the applied force F, with a velocity v, given by Stokes law:

$$v = \frac{F}{6\pi\eta r}. \qquad \text{(Equation 1)}$$

Here r is the radius of the bead, and η is the viscosity of the fluid. By knowing the viscosity of the medium in which the bead is embedded and calculating the velocity of the bead from its displacement, the force can then be determined as a function of the distance from the magnetic tip, thus providing a calibration of the apparatus and a means to independently know the applied force given the distance to the tip and the current set in the magnet.

Bead tracking

For the bead tracking, we tried to use existing image tracking solutions such as the MOSSE tracker by Bolme et al. (22) but found that these did not work well because the imaged beads had high noise with the signal limited to the low spatial frequencies. We developed a custom tracker based on a simplification of the trackers described by Bolme et al. that makes use of the radial symmetry of our beads.

We start by manually choosing the position $\mathbf{p}_0$ of a bead in the first image F_0 of an image sequence F_i. We define a function $f(F, \mathbf{p})$ that extracts an area of twice the bead radius surrounding the position $\mathbf{p}$ of an image F. This area is blurred, radially averaged, and multiplied with the Hann window function centered on the bead. For the first image, we define our matching template as $H_1 = f(F_0, \mathbf{p}_0)$ and use it to find the most likely position of our bead in the next image F_1 using

$$P_i = (H_i * F_i) \odot \mathcal{N}\left(\mathbf{p}_{i-1}, \sigma^2\right) \qquad \text{(Equation 2)}$$

which is a convolution of our template H_i with the image F_i multiplied point by point with a Gaussian $\mathcal{N}$. The Gaussian is centered on the previous position $\mathbf{p}_{i-1}$ with the width σ chosen to limit the chance of the tracking algorithm choosing a bead or more likely some other object far away from the previous position. The position of the maximum of P_i gives us the new bead position $\mathbf{p}_i$. To take into account that the illumination and shape of the bead can change from image to image, we update our template with the current image and position to

$$H_{i+1} = f(F_i, \mathbf{p}_i)\eta + H_i(1 - \eta) \qquad \text{(Equation 3)}$$

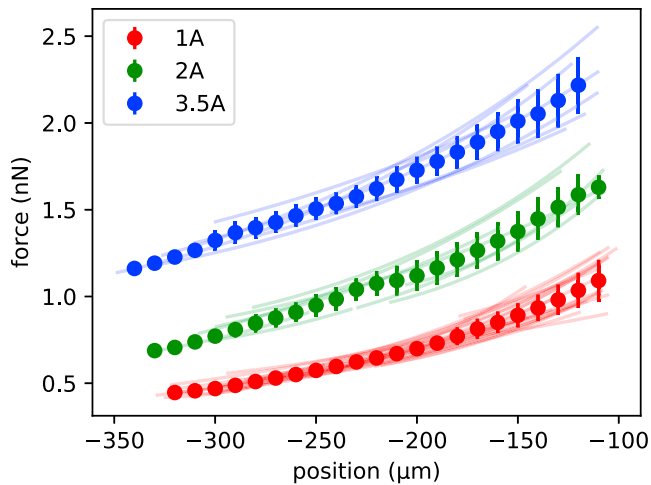where $\eta = 0.1$ is the learning rate chosen by trial and error.

FIGURE 2 Force calibration curves for 4.5-μm Dynabeads at three different current values: 1 A, 2 A, 3.5 A. Error bars are standard errors of the mean.

RESULTS

Myosin II waves on the dorsal yolk cell surface

When observing our previously generated AS-SqhKO flies, in which the pulsed Myosin II activity of the embryonic amnioserosa tissue was selectively depleted in stage 13 embryos to study its role in DC, we discovered prominent Myosin II densities that periodically formed and, in a wave-like manner, crossed the dorsal surface of the underlying yolk cell (Video S1 in the Supplementary Material). These waves could travel in all directions across the cell surface. However, many of them started off near the periphery of the visible yolk cell surface from where they preferentially traveled dorsally. The observed waves mechanically deformed the overlaying amnioserosa tissue. In a cross section view of our movies, we saw that also the yolk cell surface was considerably deformed by the passing Myosin II waves appearing to locally constrict (Fig. 3). This indicates that these Myosin II waves were contractile and exerting a function similar to the Myosin II waves in the amnioserosa cells during dorsal closure.

Myosin II waves periodicity

To characterize the dynamics of the yolk cell Myosin II waves and investigate their behavior over time, we measured their period, defined as the time between two consecutive waves, as function of time. We used an observational approach, counting the number of waves for a certain time window, as well as a quantitative approach, based on the measurement of the mean fluorescence intensity of the Myosin II waves. The timeframe was started with the beginning of the first wave, and the periodicity was calculated as the ratio between the observed timeframe and the number of detected waves, i.e., the inverse of the observed frequency of occurrence of myosin waves. We defined the "mean

observed period" as the period obtained from observation experiments and the "mean measured period" as the period calculated from the mean fluorescent signal of the Myosin II waves. In both cases, no external forces were applied.

Observation was rather trivial since the waves were prominent in most of the cases, showing themselves as flashes of fluorescent signal and therefore identified by an intensification of the fluorescence signal that subsequently shrank over time before eventually vanishing. Fig. 4 shows a Myosin II wave traveling across the surface of the yolk cell. The mean measured period of the waves was obtained by plotting the intensity profile of the Myosin II fluorescent signal, using ImageJ. Fig. 5 shows a plot of the mean fluorescence intensity profile over time. The graph looks like a periodic oscillation, where each peak corresponds to a wave. And the distance between two peaks defines the period of the waves. We observed and measured the period of the waves in 50 DC arrested stage 13 embryos. The mean observed period of the waves was 5.8 ± 0.5 min; and the mean measured period was 5.1 ± 0.4 min. The average period for different time intervals is plotted in Fig. 6: the blue curve refers to the observed periodicity and the green one to measured periodicity. At around 55 min, when wild-type embryos will roughly enter stage 14, which covers the second half of dorsal closure, we observed an apparent transition point marked by a drop in periodicity.

We checked whether the mean periodicity of the waves was the same across the entire yolk cell surface. For this purpose, we measured the mean fluorescence intensity signal in different regions of interest on the yolk cell surface (see Fig. S1). The results were always similar, regardless of where we measured, showing that there are no significant local differences.

Fluorescence measurements not only allow identifying Myosin II waves but may also provide information about the forces they exert. This is because the fluorescence intensity correlates with the number of active Myosin II molecules, which is directly related to the force magnitude assuming uniform activation of Myosin II motors. To check whether this assumption is true, one would have to compare force measurements from MT with fluorescence intensity measurements and check for a direct correlation. However, there is a considerable bias in the fluorescence measurements coming from the fluorescent signal emitted by the residual Myosin II aggregates residing in the overlying amnioserosa cells. This resulted in very small fluorescence peaks that we did not count as waves. Because these Myosin II aggregates are rather evenly distributed covering the entire yolk cell surface but obviously vary among individual embryos, it was difficult to subtract them as a noisy background to extract information about the forces exerted by the waves. To measure these forces, we instead used a MT, which allowed measuring the force exerted by a Myosin II wave in comparison to an applied magnetic force.
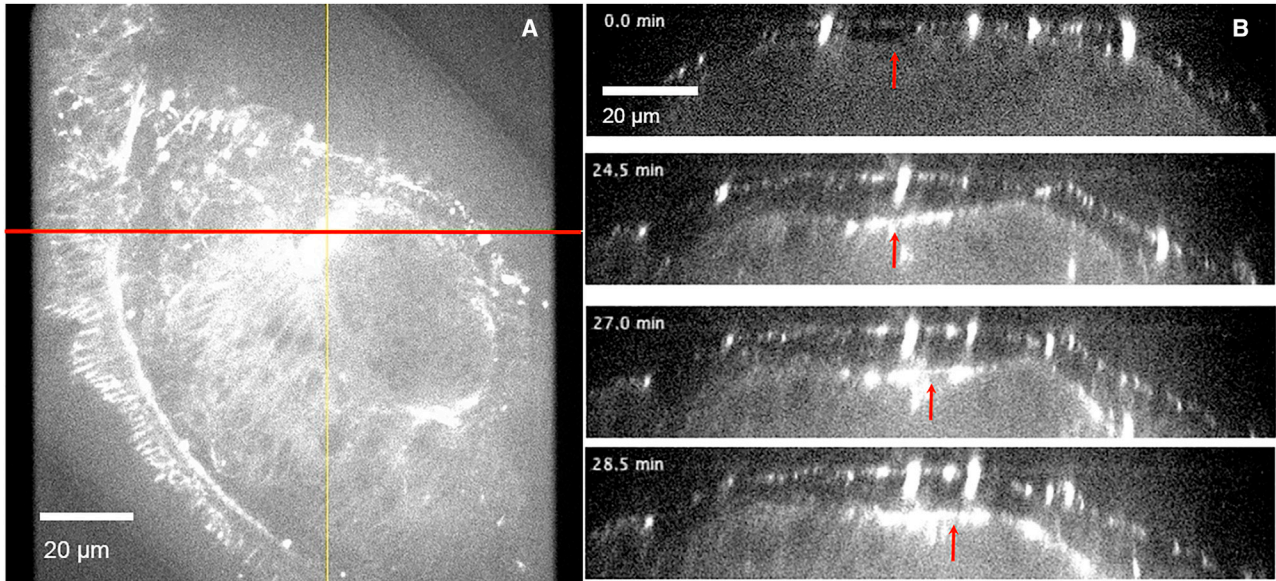
FIGURE 3 (A) z-projection of a dorsal view of a *Drosophila* embryo with fluorescently labeled Myosin II wave. The red line in (A) defines the cross-sectional view reported in (B) over time, where the deformation of the yolk cell cortex can be seen due to a passing Myosin II wave. The indentation of the yolk cortex is indicated by the red arrow over time: from top (before the wave arrives) to bottom (after the wave crossed over).

Force production by Myosin II waves

With our force calibration, we could move on to measure the forces exerted by the traveling Myosin II waves. As mentioned before, we observed local deformation of the yolk cell surface and the overlaying amnioserosa tissue when Myosin II waves passed by, indicating that the force being produced was locally contracting the cell cortex. Our strategy then was to use CAARMA to pull against these contractile forces with magnetic beads placed right below the cell cortex. In this way we could observe the bead displacement whenever a Myosin II wave moved over it. For this, single beads were injected earlier into the yolk cell of stage 5 embryos (Materials and methods). For our measurements, we pulled the magnetic bead against the yolk cell surface, with a force between 1 and 1.5 nN for about 35 min (n = 17 embryos). Fig. 7 shows a bead that was pulled dorsally against the dorsal yolk cell surface with a constant magnetic force of 1.2 nN. Myosin II waves moving over the bead then displacing it back down into the yolk cell. Beads were displaced in this way by Myosin II waves for magnetic pulling force values up to 1.5 nN. For forces of 1.6 nN and larger, beads were no longer displaced by the Myosin II waves, suggesting that the contractile forces they produce usually do not exceed 1.5 nN.

Force values of Myosin II waves

We next quantified the magnitude and range of the forces exerted by the Myosin II waves in response to an externally applied magnetic force. Again, a bead was kept pulled against the yolk cell cortex, but now we video recorded its displacement while multiple Myosin II waves passed over it. A typical trajectory of the bead is plotted as function of time in Fig. 8. The initial negative displacement of the bead was due to the external pulling force that was pointing dorsally. It is contrasted by an upward displacement induced by the Myosin II waves and then the trajectory of the bead goes up and down periodically, reflecting the periodicity of the waves. The force exerted by the Myosin II waves has a large component in the direction opposite to that of the pulling force. We calculated the force along this component as the product of the pulling force (F_p) times the ratio of the displacement induced by the waves ($\Delta X'_\mu$) and the one induced by the pulling (ΔX_p):

$$F_\mu = F_p \frac{\Delta X'_\mu}{\Delta X_p}. \qquad \text{(Equation 4)}$$

Where the subscript μ refers to the waves and p refers to the pulling. Here, we assume that the pulling force leads to an extension of the yolk cell cortex proportional to the force, i.e., in a Hookean fashion. As we will discuss in the section on the mechanical properties of the cortex, this is assumption tion is valid on the longer timescales of this type of pulling experiment, and the viscous timescale of a Kelvin-Voigt-type model describing the cortex is of the order of tens of seconds, with an elastic response on release. Therefore on the timescale of several minutes corresponding to this experiment, we can assume the cortex to be a Hookean material that is described by an effective spring constant, given by $k_{eff} = \frac{F_p}{\Delta X_p}$. Given that the Myosin II wave acts on the same material of the cortex, we therefore obtain a force of the Myosin II waves given by $F_\mu = k_{eff} \Delta X'_\mu$, which
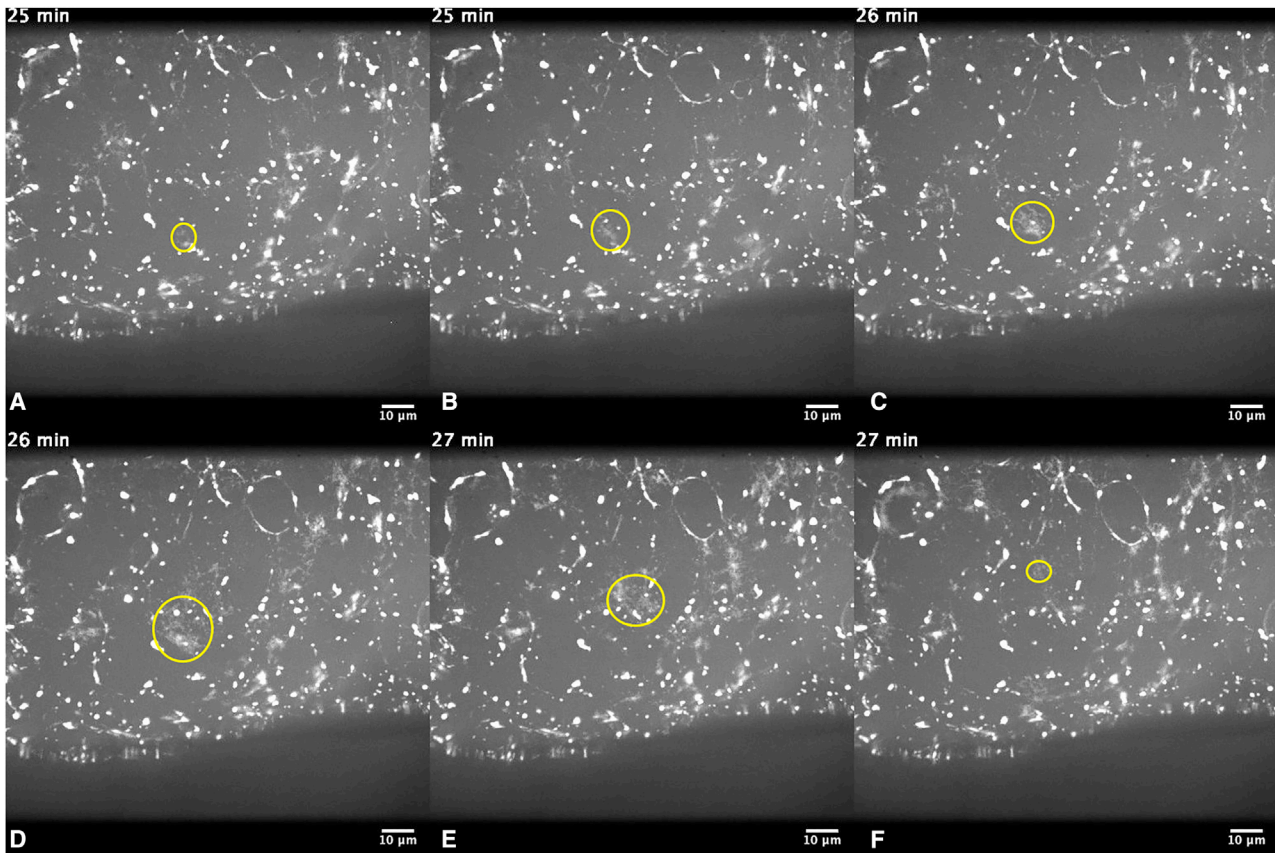
FIGURE 4 A Myosin II wave traveling across the surface of the yolk cell. The course of the wave lasts about 3 min and is shown at six subsequent time points, starting from picture (*A*) followed by (*B*), (*C*), (*D*), (*E*) and (*F*) with times indicated in the time-stamp of the frames. The bright fluorescent patches that do not change their relative position over time are Myosin II aggregates in the overlying amnioserosa cells. The encircled patches of higher intensity illustrate the growth and disappearance of a myosin wave on the yolk cell. The full time sequence of this experiment is shown in Video S2.

corresponds to Equation 4. With pulling forces ranging between 0.5 and 1.5 nN, we found a mean value of the force exerted by the Myosin II waves of 1.35 $\pm$ 0.06 nN, as an average value over 41 waves in six different embryos. We also noticed that by almost doubling the pulling force, from 0.5 nN to 1.3 nN, the force exerted by the waves increases twice and even slightly more passing from 0.63 nN to 1.50 nN.

Mechanical properties of yolk cell cytoplasm and cortex

To deliver the beads next to the yolk cell cortex in our force measurement experiments, we had to drag them toward the yolk cell surface by applying an external magnetic force. This bead traveling allowed us to investigate the viscosity of the surrounding environment using the beads as probes. The force on a small sphere moving through a viscous fluid is given by Stokes friction, Equation 1. Knowing the external magnetic force, F, as well as the radius and the velocity of the bead, the viscosity could be determined. To study the microrheological properties over time, we comple-

mented the force experiments performed in embryos at early stage 13, with experiments done at around stage 14, with the boundary empirically set where the Myosin II wave periodicity changes (see Fig. 5). Averaging over all 25 embryos covering stages 13 and 14, the mean viscosity value of the yolk cell cytoplasm was $\eta = 18.4 \pm 1.9$ Pa s. The error corresponds to the standard error of the mean. When separating the embryos into stage 13 and 14, we found a mean viscosity value of the yolk cell cytoplasm of $\eta = 11.1 \pm 2.6$ Pa s at stage 13, and of $\eta = 26.0 \pm 2.2$ Pa s at stage 14.

We next performed pulling experiments on the yolk cell cortex to study its mechanical properties. Pulling experiments basically mean that the cortex is deformed and then allowed to recoil. In this experiment, we first displaced the cortex by exerting a 30-s step force of 1.5 nN onto a 4.5-μm Dynabead, placed just below the cell cortex. The step force was chosen to be just below the threshold of 1.6 nN, for which we had found Myosin II waves not being able to compete anymore with the magnetic pulling force on the bead. We then released the force to let the cortex relax for 60 s. This was followed by a second 60-s step force of 1.5 nN, followed by a second relaxation. Fig. 9 shows the
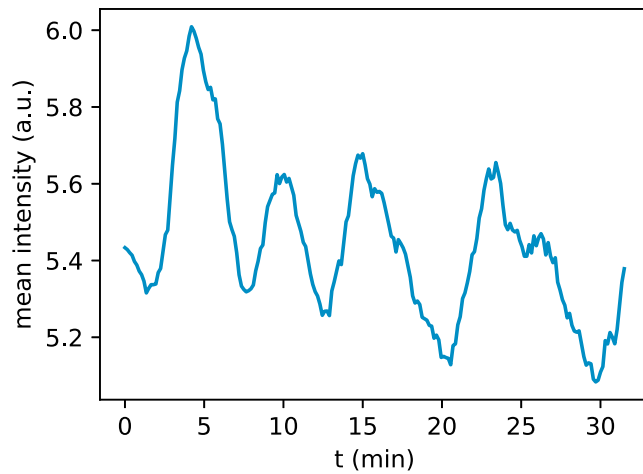
FIGURE 5　Mean fluorescence intensity profile of a Myosin II wave.

bead traces, with every trace corresponding to one experiment in one embryo. As can be seen, we observed a nearly complete recoil of the yolk cell cortex after the first pulling in most of the experiments. Interestingly, we observed a recoil that was significantly exceeding a 100% relaxation in some curves after the second pulling. Interestingly, in these cases, our preceding pulling force was not able to displace the bead as much as in the other cases. This could be explained by the influence of a Myosin II wave being present at the time of pulling, which is consistent with the fact that the timescale at which we analyze the cortex properties is comparable to that of the periodicity of the Myosin II waves. The larger extent of recoil could then be the result of the Myosin II activity displacing the bead further inside the yolk cell. Alternatively, our 60-s stretching of the cell cortex triggers an ectopic actomyosin reaction to actively counter the cortex deformation. We next used our pulling data to estimate the order of magnitude of the timescale of
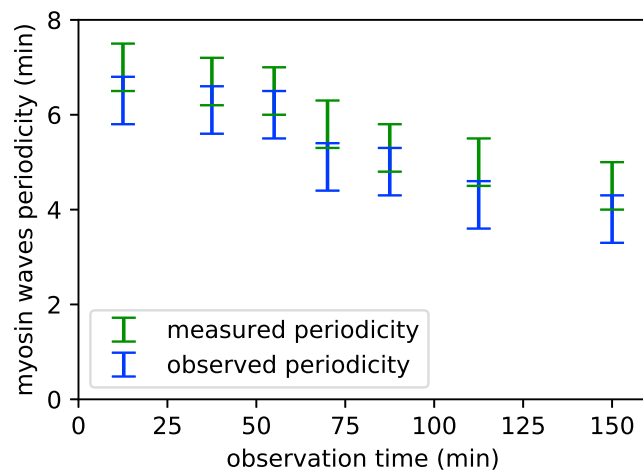

FIGURE 6　Mean observed period (blue curve) and mean fluorescent intensity period (green curve) of Myosin II waves. Error bars are standard errors of the mean.

stress relaxation for the yolk cell cortex. For this we considered only the first pulling and approximated the behavior of the cortex by the behavior of a single spring that is first stretched by a constant force for a certain time period and then released.

More specifically, we considered a spring with spring constant k, anchored at one end while the other end is connected to a bead. The instantaneous length of the spring at time t is $x(t)$, and the initial length of the spring equals its rest length x_0. We supposed a constant force F being applied to the bead during a time interval of duration T, after which the force vanishes. The total force on the bead then is the sum of the restoring force in the spring, $-k(x(t) - x_0)$, the drag on the bead from the surrounding medium, $-\eta v = -\eta \frac{dx}{dt}$ (where v is the velocity of the bead and η is the drag coefficient), and the external force applied to the bead, $F(t)$. Assuming that the mass of the bead is zero, so that inertial forces are negligible, Newton's second law implies that the total force on the bead is zero. Thus, the sum of all the forces has to be zero, and we end up with the following equation, corresponding to a Kelvin-Voigt type of material:

$$\eta \frac{dx}{dt} = F(t) - k(x(t) - x_0). \qquad \text{(Equation 5)}$$

Dividing the drag coefficient η by the spring constant k, we can define a quantity $\tau = \eta/k$ with units of time. The solution of the equation will then be $x(t) = x(0)exp(-t/\tau)$, which provides the displacement of the bead as a function of time. Therefore, if the bead is displaced by a force and then released, it shows an exponential recoil on a timescale given by τ and defined by the slope of the recoil part of the curve on a semilogarithmic plot. The mean value for τ we found was 9.9 ± 1.8 s (Fig. 10).

By knowing the timescale of cortex recoil and the viscosity of the yolk cell, we were able to estimate the elastic coefficient of the yolk cell cortex, $E = \eta/\tau$, where we found a value of $E = 1.9 ± 0.4$ Pa.

DISCUSSION

Force generation by Myosin II is responsible for powering cell division, cell motility, membrane remodeling, and embryo morphogenesis (23–27). In vitro measurements have shown that single Myosin II domains generate forces of 4–5 pN (28). In vitro optical tweezer microscopy experiments have also revealed details of the mechanism by which Myosin II generates force and provided values of the forces involved (28,29). Conversely, laser micro-dissection and traction force microscopy approaches have provided estimates for actomyosin-generated forces in living cells where many Myosin II molecules act collectively in specific subcellular locations (30,31). However, these approaches are highly invasive or require regularization parameters and
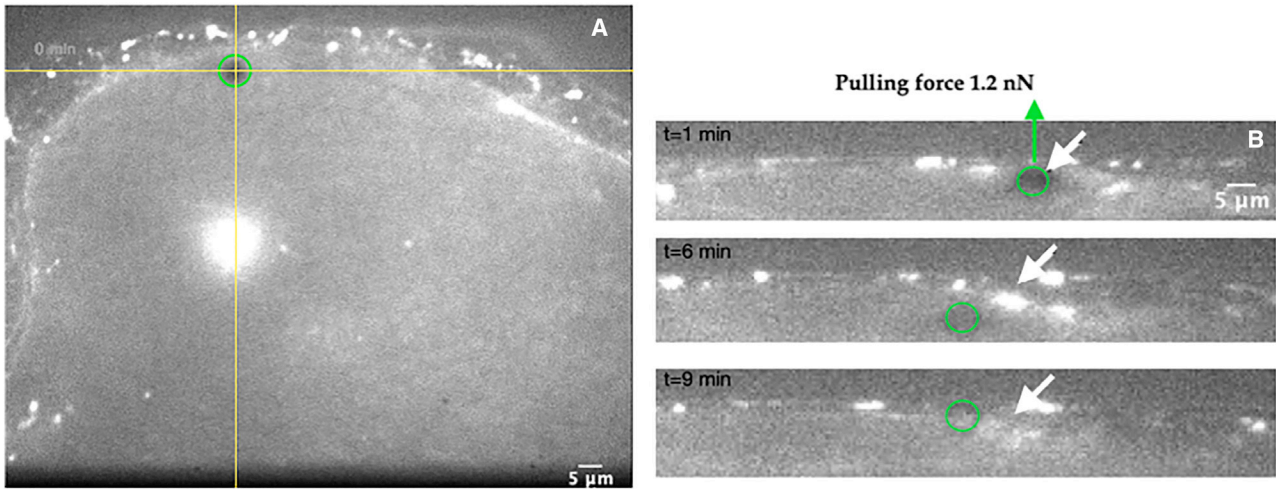
FIGURE 7   A MysoinII wave pushing back a bead (green circle) pulled against the cortex of the yolk cell with an external magnetic force of 1.2 nN. (*A*) Dorsal view of a Sqh-GFP expressing stage 13 AS-SqhKO embryo. The yellow lines depict the X-Z and Y-Z planes cutting through the bead in orthogonal views. (*B*) presents three time points of the X-Z plane in (*A*) showing how the bead is displaced by the Myosin II wave appearing on its left in the first panel and having moved across it toward the right in the middle panel. The white arrow marks the initial bead position, that in the middle panel has been displaced by the Myosin II wave, and in the third panel has settled in a new position.

consequently exhibit a substantial degree of subjectiveness. To overcome these limitations, we developed a MT system for the in vivo measurement of the mechanical forces generated by traveling waves of Myosin II on the surface of the yolk cell in *Drosophila melanogaster* embryos. With this study, we provide for the first time to our knowledge quantitative values of the forces produced by periodic cell surface Myosin II waves in a living organism.

Our work measures the forces of Myosin II waves that we detected in AS-SqhKO embryos in which we had arrested dorsal closure by acutely depleting Myosin II activity in amnioserosa cells. Consequently, the amnioserosa tissue did not deform and stayed thin, which facilitated observing the behavior of the dorsal surface of the underlying yolk cell. A developmental role for these waves remains to be shown, as they could merely be induced in response to stress imposed on the yolk cell by the abnormal behavior of the adjacent arrested amnioserosa tissue that usually on its own shows strong pulsed contractility (7). However, simultaneously with DC, two additional tissue fusion events occur below the closing epidermis and amnioserosa tissues that could well involve such yolk cell activity. First, it could support heart tube formation, during which two bilateral rows of cells migrate dorsally right behind the converging epidermis fronts to fuse and rearrange into a tube above the yolk cell (32). Similarly, midgut closure employs two tissue primordia, that laterally line the yolk cell, which at the onset of DC underlies the amnioserosa tissue (33). These cells first stretch to fuse anteriorly and
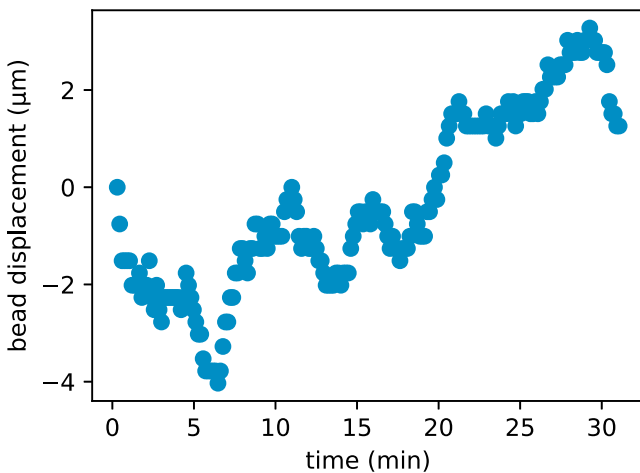

FIGURE 8   Displacement of a pulled bead under the effect of a constant force of 1.4 nN from the MT while also subjected to forces exerted by the Myosin II waves.
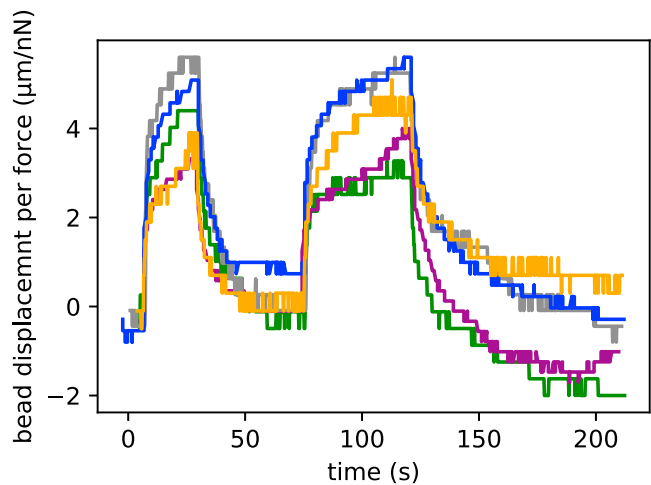

FIGURE 9   Bead traces of pulling experiments on the yolk cell cortex in five different embryos (different colors are different embryos).
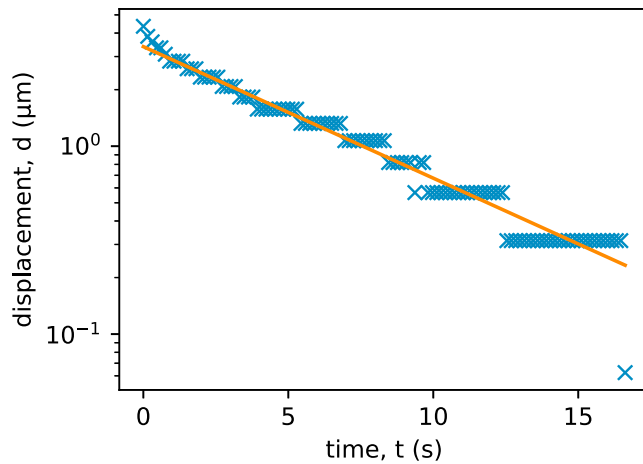
FIGURE 10 The relaxation curve of the yolk cortex after the release of a constant force applied for 30 s.

posteriorly with the ingrowing fore- and hindgut respectively. Subsequently they spread ventrally and dorsally to meet and fuse, thereby generating the midgut lumen in which the yolk cell ends up. Finally, it is also possible that yolk cell Myosin II waves support dorsal closure.

We observed that the periodicity of the Myosin II waves has a constant value until it reaches a transition time point, after which the period decreases linearly over time (Fig. 6). We define the transition time point as the passage from stage 13 to stage 14, which covers the second halve of dorsal closure, the mean period of the waves at stage 14 is about three-fourths of that at the onset of dorsal closure, for both observed and measured period values. This means that the frequency of the Myosin II waves, calculated as the inverse of the period, increases as embryonic development progresses. The frequency increase could be correlated with an increase in the overall stiffness of the yolk cell we expect during the development, showing that cellular features are not fixed even during such a short developmental period. Whether or how cellular stiffness changes affects the dynamics of Myosin II waves needs to be shown. They certainly are affected by the presence of an external force; in fact the mean periodicity value of $T = 7.7 \pm 0.6$ min found in the presence of a 1–1.5 nN magnetic force exerted to the yolk surface is about 30% larger than that found in the absence of externally applied forces.

Further, we have seen that when a Myosin II wave travels over the surface of the yolk, it induces an indentation of its cortex. If a bead is located right below the cortex area, where the wave is traveling over, then it will be pushed toward the center of the yolk regardless of the external pulling force, at least for pulling force values up to 1.5 nN. An external force from 1.6 nN will not allow the waves to compete anymore, and the bead will be not pushed by the waves. Therefore we can conclude that forces below 1.6 nN, applied to a single bead pulled against the yolk cortex, are not enough to drastically perturb the periodicity of the

waves, although they affect the force response of the Myosin II waves. Indeed, by almost doubling the pulling force, the force exerted by the waves increases by a factor of two or slightly more. For pulling force values in the range of 0.5–0.7 nN, we measured a mean force exerted by the waves of 0.63 ± 0.06 nN, and for pulling force values between 0.9 and 1.3 nN, we measured a mean force exerted by the waves of 1.50 ± 0.06 nN. The quick reaction of the Myosin II waves to the external perturbation allows the correct time-frame of embryo development. Considering that each molecular motors should exert about 5 pN, we also showed that an external magnetic force of 2.4 nN was sufficient to break the cortex membrane of the yolk cell and pass through it, as shown in Video S3.

Further, we performed experiments to characterize the physical parameters of the yolk cell, in particular the elasticity of the yolk cortex as well as the viscosity of the cytoplasm inside the yolk cell. We found a mean viscosity value of $\eta = 18.4 \pm 1.9$ Pa s. This is about 25 times larger than that of 0.75 ± 0.13 Pa s we measured in the same cell before cellularization (17), which was close to the viscosity deterimined by Wessel et al. at a similar stage. In contrast, Wessel et al. have also measured the viscosity of the yolk cell cytoplasm slightly earlier than the dorsal closure stage, in particular before the formation of the cortical layer, and found a value of $\eta = 5 \pm 2.8$ Pa s (34). The large discrepancy between our and their results for the yolk cell can be partly explained by the different developmental stage, since the viscosity increases with time due to the more complex nature of the cytoplasm as development progresses. In addition, the different techniques employed for the measurements may also play a role. By applying an external magnetic force onto a bead to infer the properties of the embedding material, we have used an active microrheology technique. Wessel et al. in contrast used a passive approach, recording the Brownian motion of a bead. Brownian motion of a bead is very small ($<1 \mu$m), being due solely to the thermal fluctuations in the medium, which becomes more of an experimental problem with increasing viscosity. Instead, we dragged the beads for tens of microns stumbling through the heterogeneous structure of the yolk cell. Therefore, our measurements are influenced by the viscosity of both fluid and internal structures, whereas passive measurements are only sensitive to the very local fluid properties. This certainly justifies a four-fold difference in viscosity values.

Finally, the relaxation dynamics displayed by the pull-and-release experiments on the cortex of the yolk cells showed that the elastic cortex restructures on a timescale of about 10 s at stage 13. This suggests that the cortex behaves elastically if deformed on a timescale shorter than 10 s, whereas it shows viscous deformation on larger timescales. Dividing the viscosity of the yolk cytoplasm by the characteristic time of cortex relaxation, we obtained a value of $E = 1.9 \pm 0.4$ Pa for the elastic modulus of the cortex. Comparing this value with the results of Doubroviniski

et al. (12), we can say that the elastic modulus of the cortex at stage 13 is about three orders of magnitude larger than at the cellularization stage. This defines a solid-like behavior of the yolk cell cortex during the dorsal closure stages 13 and 14, compared with its soft structure during the cellularization stage. We believe that the design and the approach we have established here can be applied widely to different cell types and development stages in *Drosophila* embryos as well as in other organisms, indicating that it will be a useful tool for analyzing a wide range of cell or embryo functions affected by cytoskeletal forces and importantly also for modeling purposes.

SUPPORTING MATERIAL

Supporting material can be found online at https://doi.org/10.1016/j.bpj.2021.12.038.

AUTHOR CONTRIBUTIONS

L.S., C.M.A., and D.B. designed research and wrote the article; L.S. developed CAARMA, performed experiments and analyzed data. M.A. developed the tracking software and contributed to analyze data.

ACKNOWLEDGMENTS

REFERENCES

1. Lecuit, T., and L. Le Goff. 2007. Orchestrating size and shape during morphogenesis. *Nature.* 450:189–192. https://doi.org/10.1038/nature06304.

2. Ray, H. J., and L. Niswander. 2012. Mechanisms of tissue fusion during development. *Development.* 139:1701–1711. https://doi.org/10.1242/dev.068338.

3. Begnaud, S., T. Chen, …, B. Ladoux. 2016. Mechanics of epithelial tissues during gap closure. *Curr. Opin. Cell Biol.* 42:52–62. https://doi.org/10.1016/j.ceb.2016.04.006.

4. Kiehart, D. P., J. M. Crawford, …, G. S. Edwards. 2017. Cell sheet morphogenesis: dorsal closure in Drosophila melanogaster as a model system. *Annu. Rev. Cell Dev. Biol.* 33:169–202.

5. Pasakarnis, L., E. Frei, …, D. Brunner. 2016. Amnioserosa cell constriction but not epidermal actin cable tension autonomously drives dorsal closure. *Nat. Cell Biol.* 18:1161–1172. https://doi.org/10.1038/ncb3420.

6. Eltsov, M., N. Dubé, …, A. S. Frangakis. 2015. Quantitative analysis of cytoskeletal reorganization during epithelial tissue sealing by large-volume electron tomography. *Nat. Cell Biol.* 17:605–614. https://doi.org/10.1038/ncb3159.

7. Solon, J., A. Kaya-Çopur, …, D. Brunner. 2009. Pulsed forces timed by a ratchet-like mechanism drive directed tissue movement during dorsal closure. *Cell.* 137:1331–1342. https://doi.org/10.1016/j.cell.2009.03.050.

8. Blanchard, G. B., S. Murugesu, …, N. Gorfinkiel. 2010. Cytoskeletal dynamics and supracellular organisation of cell shape fluctuations during dorsal closure. *Development.* 137:2743–2752. https://doi.org/10.1242/dev.045872.

9. Miao, H., and J. T. Blankenship. 2020. The pulse of morphogenesis: actomyosin dynamics and regulation in epithelia. *Development.* 147. https://doi.org/10.1242/dev.186502.

10. Christodoulou, N., and P. A. Skourides. 2015. Cell-Autonomous Ca2+ flashes elicit pulsed contractions of an apical actin network to drive apical constriction during neural tube closure. *Cell Rep.* 13:2189–2202. https://doi.org/10.1016/j.celrep.2015.11.017.

11. Bambardekar, K., R. Clément, …, P. F. Lenne. 2015. Direct laser manipulation reveals the mechanics of cell contacts in vivo. *Proc. Natl. Acad. Sci. U S A.* 112:1416–1421. https://doi.org/10.1073/pnas.1418732112.

12. Doubrovinski, K., M. Swan, …, E. F. Wieschaus. 2017. Measurement of cortical elasticity in Drosophila melanogaster embryos using ferrofluids. *Proc. Natl. Acad. Sci. U S A.* 114:1051–1056. https://doi.org/10.1073/pnas.1616659114.

13. Dufrêne, Y. F., A. Viljoen, …, M. Mathelié-Guinlet. 2021. AFM in cellular and molecular microbiology. *Cell Microbiol.* 23:e13324.

14. Kiehart, D. P., C. G. Galbraith, …, R. A. Montague. 2000. Multiple forces contribute to cell sheet morphogenesis for dorsal closure in Drosophila. *J. Cell Biol.* 149:471–490. https://doi.org/10.1083/jcb.149.2.471.

15. Neuman, K., and A. Nagy. 2008. Single-molecule force spectroscopy: optical tweezers, magnetic tweezers and atomic force microscopy. *Nat. Methods.* 5:491–505. https://doi.org/10.1038/nmeth.1218.

16. Conroy, R. 2008. Force spectroscopy with optical and magnetic tweezers. *In* Handbook of Molecular Force Spectroscopy. Springer https://doi.org/10.1007/978-0-387-49989-5.

17. Selvaggi, L., L. Pasakarnis, …, C. M. Aegerter. 2018. Magnetic tweezers optimized to exert high forces over extended distances from the magnet in multicellular systems. *Rev. Sci. Instrum.* 89:045106. https://doi.org/10.1063/1.5010788.

18. Fischer, J. A., E. Giniger, …, M. Ptashne. 1988. GAL4 activates transcription in Drosophila. *Nature.* 332:853–856.

19. Caussinus, E., O. Kanca, and M. Affolter. 2012. Fluorescent fusion protein knockout mediated by anti-GFP nanobody. *Nat. Struct. Mol. Biol.* 19:117–121. https://doi.org/10.1038/nsmb.2180.

20. Kiehart, D. P., J. M. Crawford, and R. A. Montague. 2007. Collection, dechorionation, and preparation of Drosophila embryos for quantitative microinjection. *Cold Spring Harb. Protoc.* https://doi:10.1101/pdb.prot4717.

21. Tanase, M., N. Biais, and M. Sheetz. 2007. Magnetic s in cell biology. *Methods Cell Biol.* 83:473–493. https://doi.org/10.1016/S0091-679X(07)83020-2.

22. Bolme, D. S., J. R. Beveridge, …, Y. M. Lui. 2010. Visual object tracking using adaptive correlation filters. *In* IEEE Computer Society Conference on Computer Vision and Pattern Recognition, pp. 2544–2550.

23. Betapudi, V. 2014. Life without double-headed non-muscle myosin II motor proteins. *Front. Chem.* 2:45.

24. Chandrasekar, I., Z. M. Goeckeler, …, P. C. Bridgman. 2014. Non-muscle myosin II is a critical regulator of clathrin-mediated endocytosis. *Traffic.* 15:418–432.

25. Milberg, O., A. Shitara, …, R. Weigert. 2017. Concerted actions of distinct nonmuscle myosin II isoforms drive intracellular membrane remodeling in live animals. *J. Cell Biol.* 216:1925–1936.

26. Sellers, J. R., M. D. Pato, and R. S. Adelstein. 1981. Reversible phosphorylation of smooth muscle myosin, heavy meromyosin, and platelet myosin. *J. Biol. Chem.* 256:13137–13142.

27. Vicente-Manzanares, M., X. Ma, …, A. R. Horwitz. 2009. Non-muscle myosin II takes centre stage in cell adhesion and migration. *Nat. Rev. Mol. Cell Biol.* 10:778–790.

28. Finer, J., R. Simmons, and J. Spudich. 1994. Single myosin molecule mechanics: piconewton forces and nanometre steps. *Nature.* 368:113–119. https://doi.org/10.1038/368113a0.

29. Spudich, J. 2001. The myosin swinging cross-bridge model. *Nat. Rev. Mol. Cell Biol.* 2:387–392. https://doi.org/10.1038/35073086.

30. Polacheck, W., and C. Chen. 2016. Measuring cell-generated forces: a guide to the available tools. *Nat. Methods.* 13:415–423. https://doi.org/10.1038/nmeth.3834.

31. Sugita, S., T. Adachi, …, M. Sato. 2011. A novel method for measuring tension generated in stress fibers by applying external forces. *Biophys. J.* 101:53–60.

32. Haack, T., M. Schneider, …, A. D. Renault. 2014. Drosophila heart cell movement to the midline occurs through both cell autonomous migration and dorsal closure. *Dev. Biol.* 396:169–182. https://doi.org/10.1016/j.ydbio.2014.08.033.

33. Tepass, U., and V. Hartenstein. 1994. Epithelium formation in the Drosophila midgut depends on the interaction of endoderm and mesoderm. *Development.* 120:579–590. https://doi.org/10.1242/dev.120.3.579.

34. Wessel, A. D., M. Gumalla, …, C. F. Schmidt. 2015. The mechanical properties of early Drosophila embryos measured by high-speed video microrheology. *Biophys. J.* 108:1899–1907. https://doi.org/10.1016/j.bpj.2015.02.032.